iScience

CellPress
OPEN ACCESS

Article

Porcine NLRC3 specially binds short dsDNA to regulate cGAS activation

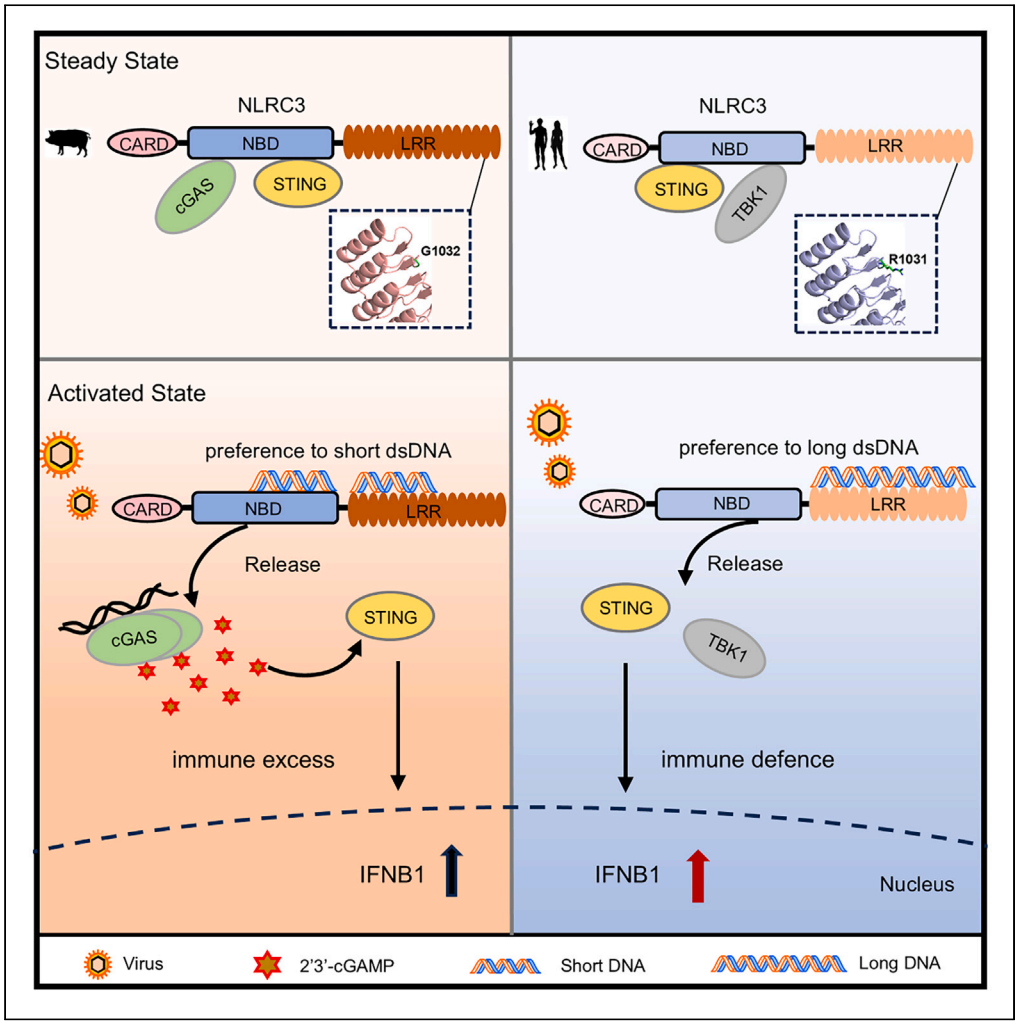

Minjie Li, Cheng Zhu, Ye Yuan, ..., Ya Yan, Pingwei Li, Xin Li

xinli2021@cau.edu.cn

Highlights

Porcine NLRC3 favors binding to short DNA via its NBD-LRR domains

A conserved arginine in LRR of porcine NLRC3 determines the preference for binding dsDNA

Porcine NLRC3 releases cGAS activation upon binding to short DNA but not long DNA

Li et al., iScience 27, 111145
November 15, 2024
https://doi.org/10.1016/j.isci.2024.111145

iScience

CellPress
OPEN ACCESS

Article

Porcine NLRC3 specially binds short dsDNA to regulate cGAS activation

Minjie Li,[1,2,5] Cheng Zhu,[3,5] Ye Yuan,[1,2] Xiangyu Huang,[1,2] Lei Wu,[1,2] Jiayang Wu,[3] Hongyan Yin,[1,2] Lvye Chai,[1,2] Weiyu Qu,[1,2] Ya Yan,[1,2] Pingwei Li,[4] and Xin Li[1,2,6,*]

SUMMARY

Host immune system has evolved multiple sensors to detect pathogenic and damaged DNA, where precise regulation is critical for distinguishing self from non-self. Our previous studies showed that NLRC3 is an inhibitory nucleic acid sensor that binds to viral DNA and thereby unleashing STING activation. In this study, we demonstrate that human NLRC3 favors long dsDNA, while porcine NLRC3 shows an affinity for shorter dsDNA. Mechanistically, a conserved arginine residue within the leucine-rich repeats of primates NLRC3 forms a structural bridge facilitating the binding of long dsDNA. Conversely, a glycine residue that replaces the arginine in non-primates disrupts this bridge. Furthermore, porcine NLRC3 negatively regulates type I interferon by interacting with cyclic GMP-AMP synthase (cGAS) to inhibit its DNA binding, thereby preventing cGAS activation. These results reveal an unrecognized mechanism by which a species-specific amino acid variation of NLRC3 influences nucleic acid recognition, providing insights into the evolution of innate immunity to pathogens.

INTRODUCTION

Innate immune system is the first line of defense against pathogens and tumorigenesis. Over decades, Toll-like receptors (TLRs), retinoic acid-inducible gene-I (RIG-I)-like receptors (RLRs), NOD-like receptors (NLRs) and other cytosolic sensors have been discovered to sense pathogen-associated molecular patterns (PAMPs) and damage-associated molecular patterns (DAMPs).[1] NLRs represent the largest family of intracellular innate immune receptors, comprising 22 proteins.[2] Inflammasomes are well-known complexes of the NLR proteins, which regulate the activation of IL-1β and IL-18.[3] Based on their association with inflammasomes, NLRs are divided into inflammasome NLRs, including NLRP1, NLRP3, NLRP6, and NLRC4, and non-inflammasome NLRs, including NLRX1, NLRC3, NLRC5, and NLRP12, which negatively regulate innate immune pathways.[4] However, there is much debate as to whether all NLRs serve as receptors for ligands, particularly since most NLR ligands are bacterial in origin. For example, the ligands for NOD1 and NOD2 are bacterial peptidoglycans[5–8] and lipoteichoic acid (LTA) is the ligand for NLRP6.[9] NAIPs (neuronal apoptosis inhibitory proteins) bind to type III secretion system (T3SS) proteins and induces NLRC4 inflammasome activation.[10] Contrary to bacterial ligands, the LRR domain of NLRX1, which is rich in positive charged residues, specifically binds dsRNA.[11,12] Most nucleic acid sensors possess a specificity for DNA or RNA of different lengths. For example, retinoic acid-inducible gene-I (RIG-I) and melanoma differentiation-associated gene 5 (MDA5) preferentially recognize short and long dsRNA, respectively.[13,14] Absent-in-melanoma-2 (AIM2) and interferon-inducible protein 16 (IFI16) bind dsDNA in a length-dependent manner, which assemble with longer dsDNA to oligomerize in filament formation.[15,16] Cyclic GMP-AMP synthase (cGAS) is another dsDNA sensor, which senses long dsDNA inducing oligomerization and liquid phase separation in a length-dependent manner.[17,18] NLRC3 is an inhibitory sensor that negatively regulates multiple signaling pathways, including nuclear factor kappa B (NF-κB),[19,20] type I interferon (IFN-I),[21] and mammalian target of rapamycin (mTOR) pathways.[22] Besides the inhibitory function, we discovered NLRC3 directly binds to herpes simplex virus (HSV-1) dsDNA with high affinity.[23] However, NLRC3 from other species have not been reported except the fish, which impedes evolutionary knowledge of this subgroup of inhibitory NLRs. In addition, it is not known the binding properties of DNA sensor from other species and whether DNA binding in a length-dependent manner is evolutionarily conserved. Here, we present the findings that porcine NLRC3 (pNLRC3) directly interacts with dsDNA via its NBD-LRR domain, unlike its human counterpart. Strikingly, pNLRC3 exhibits a preference for short DNA, a stark contrast to human NLRC3 (hNLRC3) which preferentially binds long DNA. Mechanistically, an arginine (R) residue in the LRR 13–16 is evolutionarily conserved in primates that formed a bridge to associate with long dsDNA, while in non-primates, this arginine residue is replaced by a glycine (G) residue that disrupts the bridge. Interestingly, swapping these amino acids through either "R to G" or "G to R" mutations inverse the DNA

[1]National Key Laboratory of Veterinary Public Health and Safety, China Agricultural University, Beijing 100193, China
[2]Key Laboratory of Animal Epidemiology of the Ministry of Agriculture and Rural Affairs, College of Veterinary Medicine, China Agricultural University, Beijing, China
[3]Tianjin Key Laboratory of Function and Application of Biological Macromolecular Structures, School of Life Sciences, Tianjin University, Tianjin 300072, China
[4]Department of Biochemistry and Biophysics, Texas A&M University, College Station, TX, USA
[5]These authors contributed equally
[6]Lead contact
*Correspondence: xinli2021@cau.edu.cn
https://doi.org/10.1016/j.isci.2024.111145

binding propensities of hNLRC3 and pNLRC3. Mechanistically, the NBD of pNLRC3 interacts with catalytic domain of cGAS and prevents its activation by dsDNA. Furthermore, pNLRC3 releases bound cGAS upon association with short DNA but not long DNA. In summary, this study provides critical insights into the evolution of immune sensors, demonstrating how a single amino acid residue influences the preference of DNA binding by primates and non-primates NLRC3, providing critical insight into the evolution of the innate immune system.

RESULTS

Porcine NLRC3 binds to viral DNA via its NBD and LRR domain

NLRC3 is an inhibitory NLR that directly binds to viral DNA because the LRR domain of NLRC3 is rich in positive charged amino acids that interacts with dsDNA through electrostatic interaction.[23] We detected the expression of pNLRC3 in multiple tissues including tonsil, spleen, bone marrow, and thymus by qPCR and amplified full-length pNLRC3 ($pNLRC3^{FL}$) in spleen (Figures S1A and S1B). Then, we aligned the amino acid sequences of pNLRC3 with hNLRC3 and the results showed CARD, NBD, and LRR domain of pNLRC3 shared homology of 80.7%, 82.45%, and 88.17% with those of hNLRC3, respectively (Figures 1A and S2). To understand DNA binding by pNLRC3 at molecular level, we predicted the structure of pNLRC3 by AlphaFold and the predicted structure showed a number of positive charged amino acids distributed among NBD and LRR, which are likely involved in dsDNA binding (Figure 1B). To determine the DNA binding domain of pNLRC3, we cloned $pNLRC3^{FL}$ and various truncations including $pNLRC3^{CARD}$, $pNLRC3^{CARD-NBD}$, $pNLRC3^{NBD}$, $pNLRC3^{NBD-LRR}$, and $pNLRC3^{LRR}$, then verified the interaction with dsDNA by pull-down (Figures 1A and S3). To test if pNLRC3 binds to DNA directly, biotinylated-HSV60 dsDNA co-precipitated with hemagglutinin (HA)-tagged pNLRC3 and showed that it efficiently precipitated pNLRC3 and the positive controls hNLRC3, human cGAS (hcGAS) but not RNA-binding protein human RIG-I (hRIG-I) in HEK-293T cells (Figure 1C). To further probe the DNA binding domains of pNLRC3, $pNLRC3^{FL}$, $pNLRC3^{CARD}$, $pNLRC3^{CARD-NBD}$, $pNLRC3^{NBD}$, $pNLRC3^{NBD-LRR}$, $pNLRC3^{LRR}$ were transfected into HEK-293T cells. Biotinylated-HSV60 dsDNA co-precipitated with $pNLRC3^{FL}$, $pNLRC3^{CARD-NBD}$, $pNLRC3^{NBD}$, $pNLRC3^{NBD-LRR}$, $pNLRC3^{LRR}$ but not $pNLRC3^{CARD}$ (Figure 1D). These results showed that the NBD and LRR domain contribute to DNA binding by pNLRC3, while only the LRR is involved in DNA binding by hNLRC3. To test whether pNLRC3 and hNLRC3 also bind to DNA/RNA hybrids and dsRNA, biotinylated-HSV60 DNA/RNA hybrids and HSV60 dsRNA co-precipitated with $pNLRC3^{FL}$ and $hNLRC3^{FL}$. The results showed that both pNLRC3 and hNLRC3 interacted with DNA/RNA hybrids and dsRNA (Figures 1E and 1F). To test whether $pNLRC3^{FL}$ directly binds to DNA, we constructed a cell line stably expressing GFP-Strep-II-pNLRC3 in HEK-293T cells using PiggyBac Transposase system and the fluorescence of GFP indicated the insertion of pNLRC3 (Figure S4A). Subsequently, $pNLRC3^{FL}$ recombinant proteins were purified by strep resins and followed by SDS-PAGE and western blot (Figures S4B and S4C). Furthermore, we expressed $pNLRC3^{NBD}$ and $pNLRC3^{LRR}$ proteins in *E. coli*. The $pNLRC3^{NBD}$ proteins were purified by glutathione resin (Figure S4D). The $pNLRC3^{LRR}$ proteins were purified by Ni-NTA and followed by size exclusion chromatography (Figures S4E and S4F).

Pull-down assay showed purified $pNLRC3^{FL}$, $pNLRC3^{NBD}$, and $pNLRC3^{LRR}$ recombinant proteins directly bind to HSV60 dsDNA, consistent with the pull-down results in cells (Figures 1G–1I). Collectively, these results showed that pNLRC3 directly binds to dsDNA, DNA/RNA hybrid and dsRNA via its NBD and LRR domains.

Human and porcine NLRC3 prefer dsDNA of different lengths

cGAS is activated by dsDNA in a length-dependent manner,[18,24] and small cytoplasmic dsDNA, but not long dsDNA, represses cGAS activation and induces autophagy.[25] In addition, other DNA sensors, for example, AIM2 and IFI16 also bind to dsDNA in a length-dependent manner.[15,16] Previously, we reported hNLRC3 LRR 1–4 and LRR 13–16 bind to HSV60, while HSV15 only binds to hNLRC3 LRR 1–4 (Figure 2A). To investigate whether pNLRC3 also binds to DNA in a length-dependent manner, we simulated the interactions between pNLRC3 with 15 bp, 30 bp, and 60 bp dsDNA using all-atom molecular dynamics. The simulations showed that shorter strands (HSV15 and HSV30) tightly associated with the NBD and LRR 1–4 of pNLRC3 (Figures 2B and S5A–S5C), while the longer strands (HSV60) detached from pNLRC3 in >50% frames throughout the 100 ns trajectories (Figure 2C). The average distance between pNLRC3 and HSV15 was 8.31 $\pm$ 0.28 Å, while the systems with HSV60 featured larger and fluctuating distance, which was 54.71 $\pm$ 2.33 Å (Figures 2D and 2E), indicating lower affinities between pNLRC3 and longer DNA strands. To determine the affinity of the pNLRC3 protein with different lengths of DNA, we used GFP-pNLRC3 as the target and performed microscale thermophoresis (MST) assays with HSV30, HSV60, and HSV120, respectively. The results showed binding affinities were 1.6 μM, 5.7 μM, and 10.1 μM, indicating that pNLRC3 has a higher affinity for short dsDNA (Figure 2F). We applied various lengths of biotinylated-HSV15, 30, 60, and 120 bp dsDNA in pull-down to compare the DNA binding properties of $pNLRC3^{FL}$ and $hNLRC3^{FL}$, respectively. Indeed, pNLRC3 recognizes short dsDNA or DNA/RNA hybrids, while hNLRC3 prefers binding to long dsDNA and DNA/RNA hybrids in a length-dependent manner (Figures 2G–2J). Taken together, these results indicate a species-specific preference of NLRC3, with pNLRC3 specializing in the recognition of short dsDNA through its NBD-LRR domains, distinct from the preference of long dsDNA of hNLRC3.

The replacement of a single residue within LRR 13–16 determines the preference of different dsDNA by NLRC3

To explore the molecular mechanism underlying the preference of pNLRC3 toward short DNA strands, we compared the electrostatic surface between pNLRC3 and hNLRC3. The positive-charge enriched area (Figure 3A bottom, blue color) usually mediated high-affinity and low-specificity associations between proteins and nucleic acids. hNLRC3 featured two positive charged surface patches at LRR 1–4 and LRR 13–16 regions, both of which contributed to the recognition of relatively long DNA strands.[23] In contrast, pNLRC3 featured only one such

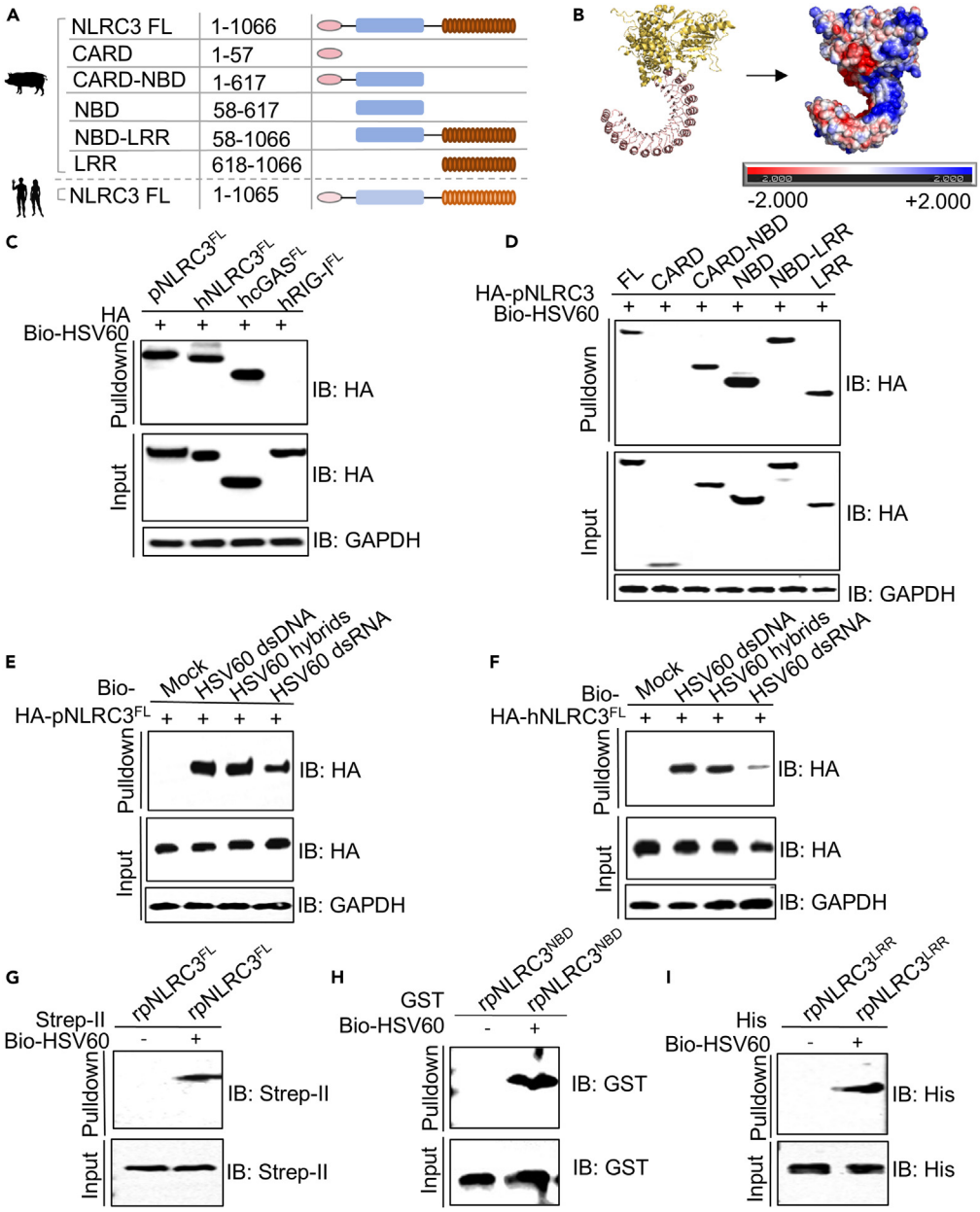

Figure 1. Porcine NLRC3 binds to viral DNA via NBD and LRR domain

(A) Schematics view of the domain architecture of porcine and human NLRC3.

(B) Electrostatic potential surface maps of pNLRC3^{FL} by AlphaFold (blue represents positive charge enriched area, red represents negative charge enriched area).

(C) Streptavidin pull-down assay of HA-pNLRC3^{FL}, HA-hNLRC3^{FL}, HA-hcGAS^{FL} and HA-hRIG-I^{FL} in HEK-293T cells. The whole cell lysate for streptavidin pull-down was incubated with biotin-HSV60. HA-hNLRC3^{FL} and HA-hcGAS^{FL} serve as positive controls, and HA-hRIG-I^{FL} is a negative control.

(D) Streptavidin pull-down assay for the binding of biotin-HSV60 dsDNA to HA-pNLRC3^{FL} or indicated domains of pNLRC3 in HEK-293T cells.

(E and F) Streptavidin pull-down assay of HA-pNLRC3^{FL}(E) and HA-hNLRC3^{FL}(F) binding to biotin-HSV60 dsDNA, biotin-HSV60 DNA-RNA hybrids and biotin-HSV60 dsRNA.

(G–I) Streptavidin pull-down assay for the binding of biotin-HSV60 dsDNA to Strep-II-pNLRC3^{FL} (G), GST-pNLRC3^{NBD}(H) and His-pNLRC3^{LRR} (I) recombinant proteins.

site at LRR 1–4 (Figures 2B and 2C). Hence, we hypothesized the lack of charged residues (e.g., arginine) at LRR 13–16 may lead to the altered preference of pNLRC3 toward short DNA. Indeed, we identified a mutation in the LRR 13–16 region (G1032 for pig and R1031 for human, Figure 3A middle). To explore the evolutionary significance of these residues, we constructed a phylogenetic tree to analyze full-length NLRC3 sequences across species. The results showed the gene of NLRC3 evolved from Zebrafish and was highly homologous among

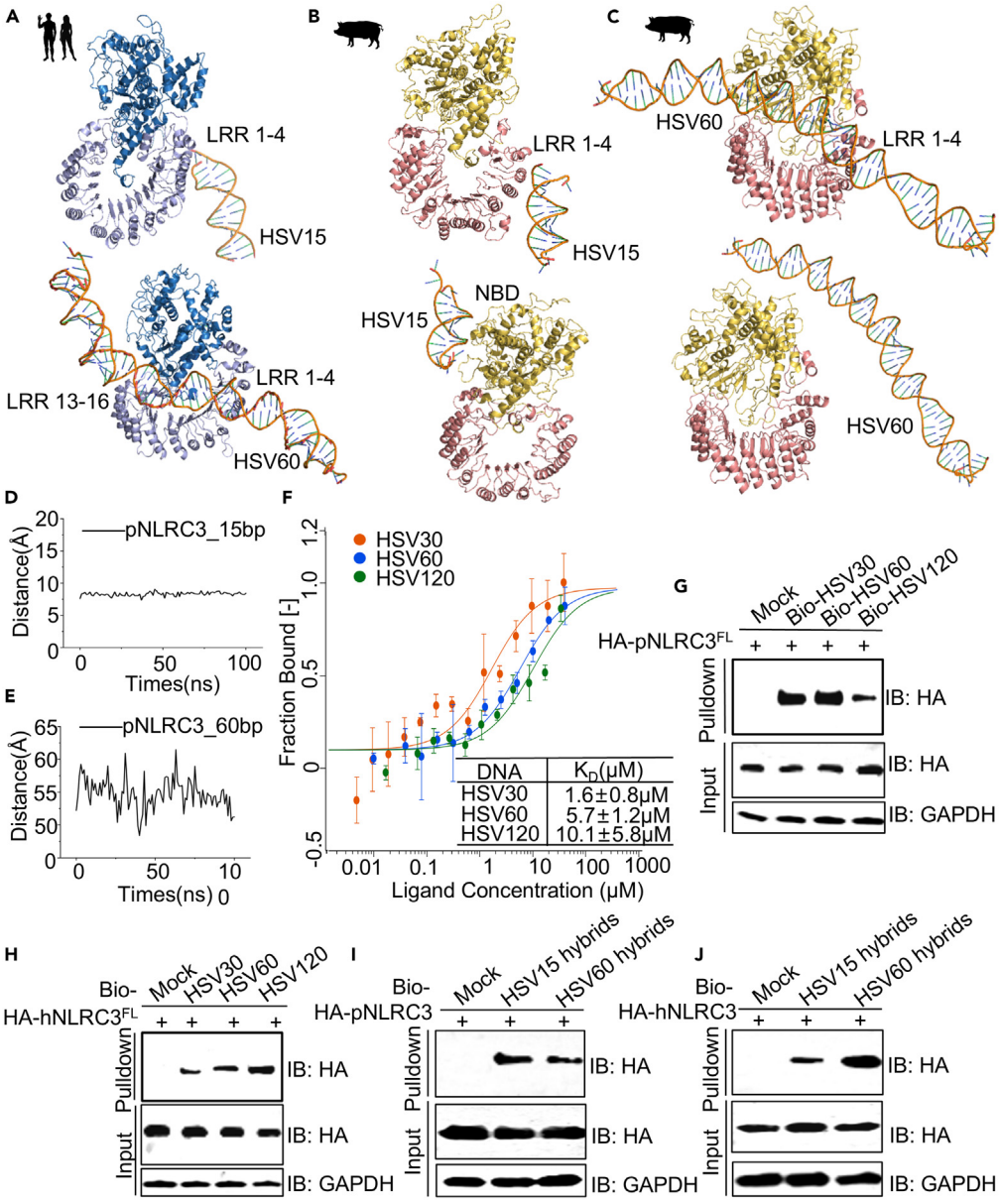

Figure 2. Human and porcine NLRC3 prefer different lengths of dsDNA

(A) Computationally derived binding model of hNLRC3 NBD-LRR with HSV15 (upper) and HSV60 (bottom) dsDNA. hNLRC3, NBD is highlighted in blue, and LRR is highlighted in purple.

(B and C) Computationally derived binding model of pNLRC3 NBD-LRR with HSV15 (B) and HSV60 (C) dsDNA. The binding conformations between pNLRC3 and dsDNA were derived from all-atom MD simulations at the equilibrium states. HSV15 associated with either NBD or LRR domains, while HSV60 dissociated from pNLRC3 (distance >50 Å) in representative conformations suggesting weaker affinities. pNLRC3, NBD is highlighted in yellow, and LRR is highlighted in pink.

(D and E) The distance between 15 bp dsDNA (D) or 60 bp dsDNA (E) and pNLRC3 was estimated by measuring the distance between pNLRC3 and DNA backbone atom.

(F) MST assays showing pNLRC3 binding affinities with HSV30, HSV60 and HSV120. Each experiment was independently repeated three times.

(G and H) Streptavidin pull-down assay for the binding of biotin-HSV30, biotin-HSV60 and biotin-HSV120 dsDNA to HA-pNLRC3^{FL} (G) or HA-hNLRC3^{FL} (H) transfected in HEK-293T cells.

(I and J) Streptavidin pull-down assay of HA-pNLRC3^{FL}(I) and HA-hNLRC3^{FL}(J) binding to biotin-HSV15 DNA/RNA hybrids and biotin-HSV60 DNA/RNA hybrids.

different organisms, possibly originating from invertebrate. The alignments of the amino acids among different species of NLRC3 were conserved and the sequences of primates formed a separate clade (blue) (Figure 3B). To further explore the conservation of hNLRC3 R1031 and pNLRC3 G1032 among species, a single amino acid sequence alignment was performed at site R1031 in hNLRC3 (refer to pNLRC3

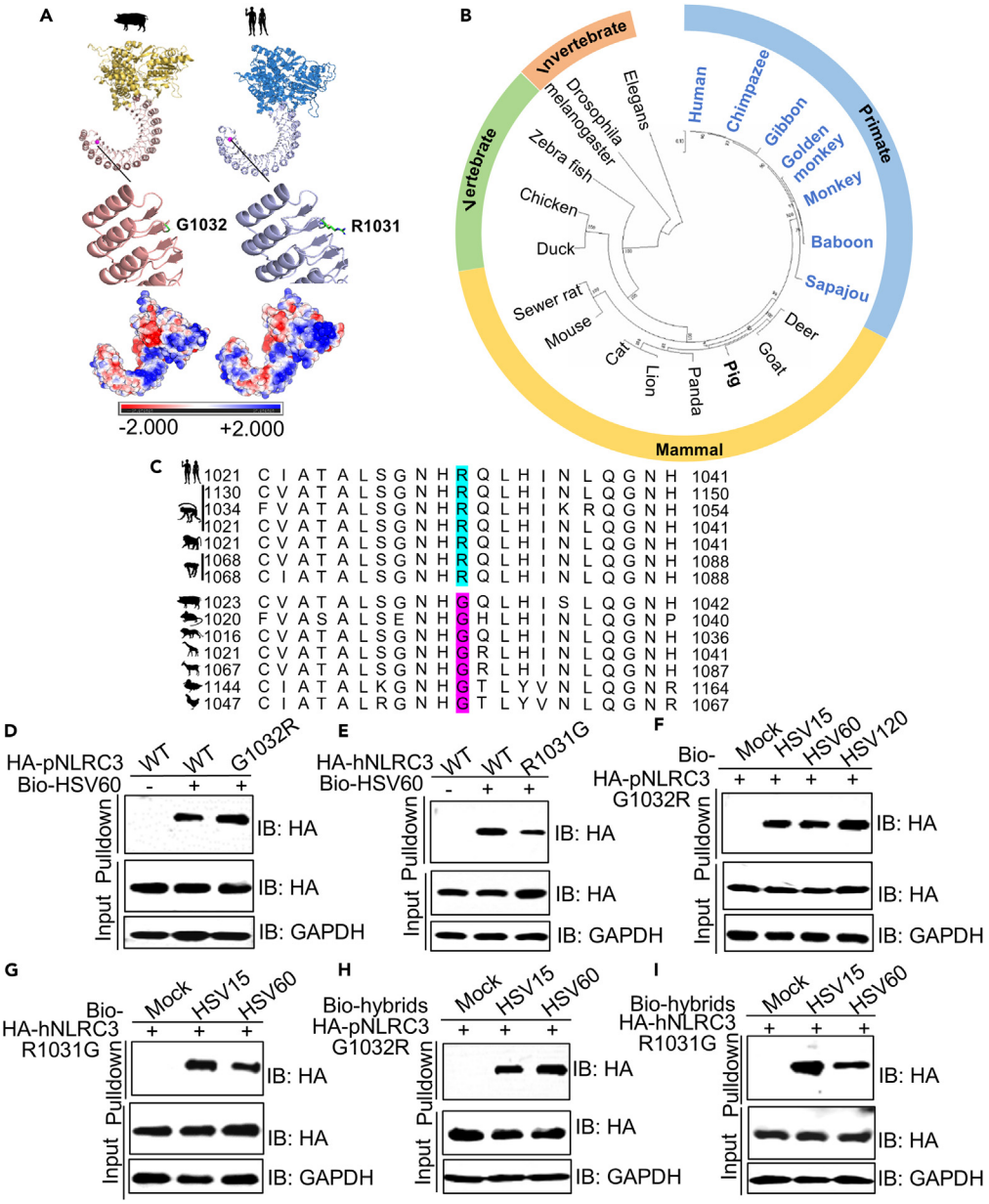

Figure 3. The replacement of a single residue within LRR 13-16 determines the preference of different dsDNA by NLRC3

(A) The three dimensional structure (upper) and electrostatic potential surface maps(bottom) alignment of the NBD and LRR domain of pNLRC3 and hNLRC3.

(B) Phylogenetic analysis of NLRC3 proteins in different species including invertebrate and vertebrate. The tree was drawn to scale, with branch lengths in the same units as those of the evolutionary distances used to infer the phylogenetic tree. The evolutionary distances were computed using the p-distance method. Evolutionary analyses were conducted in MEGA7.

(C) The amino acid sequence alignment of pNLRC3 G1032 site in 14 different species.

(D and E) Streptavidin pull-down assay of HA-pNLRC3^{FL} WT and G1032R mutant (D) or HA-hNLRC3^{FL} WT and R1031G mutant (E) binding to biotin-HSV60.

(F and G) Streptavidin pull-down assay for the binding of different lengths biotin-dsDNA to HA-pNLRC3 G1032R mutant (F) and HA-hNLRC3 R1031G mutant (G).

(H and I) Streptavidin pull-down assay for the binding of different lengths biotin-DNA/RNA hybrids to HA-pNLRC3 G1032R mutant (H) and HA-hNLRC3 R1031G mutant (I).

at G1032). Surprisingly, all the primates showed an R at 1031, however, non-primates displayed a G (Figure 3C). To further verify the conservation of R1031 in primates, we aligned thirteen species in primates, including human, monkey, baboon, and orangutan, which showed R1031 was completely conserved indicating a uniform feature in primates (Figure S6). Since R is positive charged, while G is uncharged, which may explain why hNLRC3 has a higher affinity for long dsDNA. To test this hypothesis, the mutants of pNLRC3 G1032R and hNLRC3 R1031G were

constructed to precipitate with various lengths of dsDNA by pull-down assay. Interestingly, we observed that the pNLRC3 G1032R mutation enhanced the protein's capacity to bind long dsDNA, whereas the hNLRC3 R1031G mutation decreased this binding compared to wild-type (WT) control (Figures 3D and 3E). To further confirm whether the interaction between NLRC3 and dsDNA is length-preference, pNLRC3 G1032R and hNLRC3 R1031G mutants were subjected to pull-down assays with HSV15, HSV60, and HSV120. Indeed, pNLRC3 G1032R exhibited a preference for longer dsDNA strands in a length-dependent manner, whereas hNLRC3 R1031G displayed stronger binding to HSV15 compared to HSV60, suggesting the important role of this conserved R/G residue in the recognition of dsDNA of different lengths (Figures 3F and 3G). Consistently, pNLRC3 G1032R variant showed an increased affinity for longer nucleic acid hybrids, contrasting with the hNLRC3 R1031G variant which favored shorter hybrids (Figures 3H and 3I). Taken together, the replacement of an arginine residue by glycine in NLRC3 LRR 13–16 distinguishes the preference for DNA of different lengths in primates and non-primates.

Porcine NLRC3 negatively regulates IFN-I induction by interacting with cGAS and STING

hNLRC3 inhibits IFN-I induction by interacting with STING and TBK1 via the NBD domain.[21] To investigate whether pNLRC3 affects signal transduction of the cGAS-STING pathway, we detected IFN-β promoter activity by overexpressing pNLRC3 in HEK-293T cells. The results indicated that pNLRC3 significantly suppressed IFN-β promoter activation by cGAS, STING, TBK1, and IRF3 (Figures 4A, S7A, and S7B). To further explore the inhibitory effect of pNLRC3, we overexpressed and knocked down pNLRC3 in PK-15 cells and immortalized PAMs (PAM-Tang) cells upon poly(dA:dT) stimulation. The results showed that overexpressing pNLRC3 remarkably suppressed the mRNA level of IFN-β and RNAi of pNLRC3 promoted the mRNA level of IFN-β in PK-15 and PAM-Tang cells upon transfection of poly(dA:dT) (Figures 4B and 4C). The results were consistent in HeLa cells (Figure 4D). Furthermore, pNLRC3 also reduced IFN-β production upon stimulation by 2′,3′-cGAMP, suggesting an inhibitory role in STING-mediated signaling (Figure 4E). To explore whether pNLRC3 interacts with porcine cGAS (pcGAS), STING (pSTING), TBK1 (pTBK1), and IRF3 (pIRF3), we co-transfected Flag-pNLRC3 with HA-pcGAS, HA-pSTING, and HA-pIRF3 or Flag-pTBK1 with HA-pNLRC3 in HEK-293T cells, respectively. Co-immunoprecipitation (Co-IP) showed pNLRC3 efficiently precipitated with pcGAS and pSTING (Figures 4F and 4G) but not pTBK1 and pIRF3 (Figure S7C and S7D). In addition, we performed confocal microscopy to visualize the co-localization of pNLRC3 with pcGAS and pSTING in HEK-293T cells and pIRF3 was as a negative control (Figures 4H, 4I, and S7E). Previous results have showed hNLRC3 interacts with human STING (hSTING) and TBK1 (hTBK1).[21] We confirmed the interaction between hNLRC3 and hSTING, however, we did not observe the interaction between hNLRC3 and human cGAS (hcGAS) (Figures S8A and S8B). Collectively, these results suggest pNLRC3 negatively regulates IFN-I induction through cGAS and STING.

Porcine NLRC3 interferes with DNA binding and inhibits the activation of cGAS

Previous studies showed that hNLRC3 interacts with hSTING and hTBK1 but not hcGAS. To explore the new roles of pNLRC3 in cGAS regulation, we generated constructs of various domains of pNLRC3 (CARD, NBD, and LRR) and pcGAS (NT and CT) and tested their interactions in cells (Figure 5A). The NBD domain of pNLRC3 showed a strong association with pcGAS and pSTING (Figures 5B and 5C). pNLRC3 specially precipitated with pcGAS^{CT} but not pcGAS^{NT} (Figures 5D and 5E). To further confirm these results, pNLRC3^{NBD} and pcGAS^{CT} were co-expressed in HEK-293T cells and Co IP showed that pNLRC3^{NBD} interacted with pcGAS^{CT} (Figure 5F). These results suggested that pNLRC3 NBD likely blocks DNA binding by cGAS and inhibits its enzymatic activity. As nucleic acid receptors, both pNLRC3 and pcGAS can interact with dsDNA to mediate innate immune responses. To explore whether pNLRC3 affects the binding of pcGAS and dsDNA, we performed a competitive pull-down assay. The results showed that the addition of pNLRC3 significantly reduced the interaction between pcGAS and dsDNA (Figure 5G), indicating pNLRC3 competes with pcGAS in DNA binding. cGAS is activated by dsDNA and produces 2′,3′-cGAMP, which is essential to activate STING-mediated signaling.[26] To probe whether pNLRC3 affects the catalytic activity of pcGAS, we expressed and purified pcGAS recombinant proteins in *E. coli* as previous protocol.[27] Subsequently, we set up an enzymatic assay to detect the production of 2′,3′-cGAMP using a Mono Q ion-exchange column (black peak) as our previous study.[27] Next, we added pNLRC3^{FL} or pNLRC3^{LRR} proteins in this enzymatic system, respectively. The results showed that the level of 2′,3′-cGAMP was significant reduced after adding pNLRC3^{FL} (orange peak) or pNLRC3^{LRR} (blue peak) proteins (Figure 5H). In addition, pNLRC3^{FL} exhibited a stronger inhibitory effect than pNLRC3^{LRR} on cGAS enzymatic activity. Taken together, these results demonstrate that pNLRC3 interferes with DNA binding and inhibits the enzymatic activity of cGAS.

Porcine NLRC3 facilitates the activation of cGAS by binding short dsDNA

Our previous work demonstrated that viral DNA binding to hNLRC3 unleashes STING and TBK1 activation. To determine whether viral DNA binding to pNLRC3 results in pcGAS activation, HSV60 and HSV30 dsDNA was added to the intact cell lysates of co-transfected pNLRC3 and pcGAS in HEK-293T cells by immunoprecipitation, respectively. The results suggested that HSV60 did not affect the interaction of pNLRC3 with pcGAS (Figure 6A). However, we observed that HSV30 prevented pcGAS from pNLRC3 inhibition in a dose dependent manner (Figure 6B). Furthermore, we performed similar experiment on the interaction of pNLRC3 with porcine STING (pSTING) by adding HSV60 or HSV30. Surprisingly, pSTING unleashed from pNLRC3 was triggered upon HSV30 addition but not by HSV60 (Figures 6C and 6D). These results demonstrate pNLRC3's marked affinity for short dsDNA that hampers its interaction with proteins, such as cGAS and STING. In addition, we conducted pcGAS enzymatic activity assay using HSV60. We observed pNLRC3 G1032R (green peak) produced more 2′,3′-cGAMP than WT (orange peak), suggesting the weaker inhibition of pNLRC3 G1032R of cGAS. Because pNLRC3 G1032R exhibits enhanced HSV60 binding, thus reducing its inhibition of cGAS (Figure 6E). Similarly, we detected the effects of hNLRC3 WT and R1031G on hcGAS enzymatic

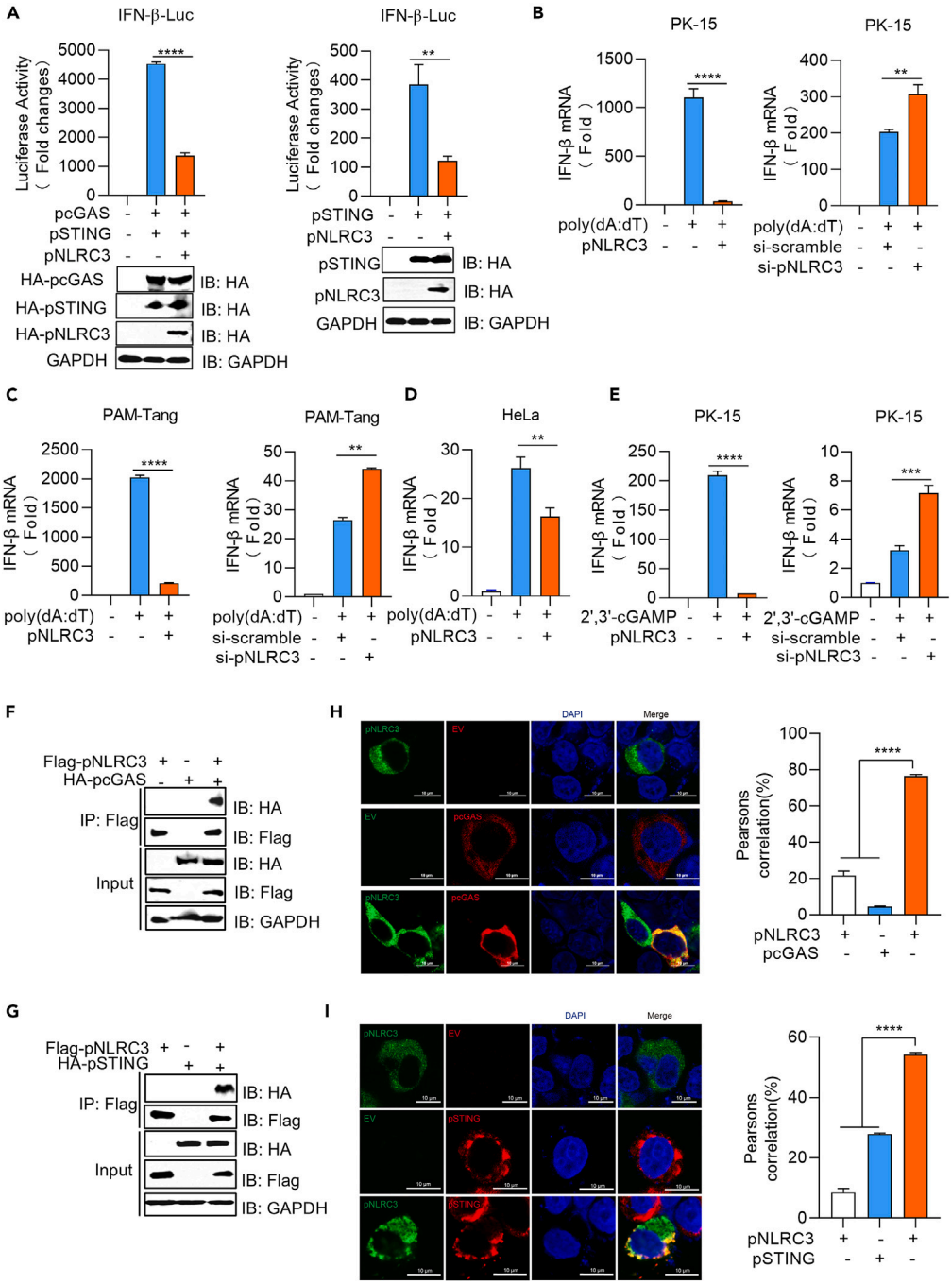

Figure 4. Porcine NLRC3 negatively regulates IFN-I via interacting with cGAS and STING

(A) Luciferase assay was performed to detect the effects of pNLRC3^{FL} overexpression on the activation of IFN-β promoter triggered by cGAS-STING. HEK-293T cells were transfected with an IFN-β-Luc reporter plasmid, plus expression plasmids for pNLRC3^{FL}, pcGAS and pSTING for 24 h before luciferase assay. Statistics indicate significance by Two-tailed unpaired t-test: ****$p < 0.0001$, ***$p < 0.001$, **$p < 0.01$, *$p < 0.05$; ns, not significant.

(B–E) RT-qPCR experiments were performed to determine the effects of pNLRC3^{FL} overexpression or knock down with siRNA on poly(dA:dT) triggered IFN-β production in PK-15 (B), PAM-Tang (C) and HeLa cells (D). PK-15 cells were stimulated with 2′,3′-cGAMP as indicated, and IFN-β levels were determined after stimulation (E). All data are depicted as mean ± SD of three independent experiments.

(F and G) Anti-Flag immunoprecipitates of HA-pcGAS (F) and HA-pSTING (G) with Flag-pNLRC3 in HEK-293T cells. The cell lysates and immunoprecipitates were analyzed by immunoblotting as indicated.

(H and I) The confocal microscopy analysis of co-localization between Flag-pNLRC3 (green) and HA-pcGAS (red) (H) or HA-STING (red) (I) in HEK-293T cells. Nuclei was stained with 4′,6-diamidino-2-phenylindole (DAPI). Scale bars represent 10 μm.

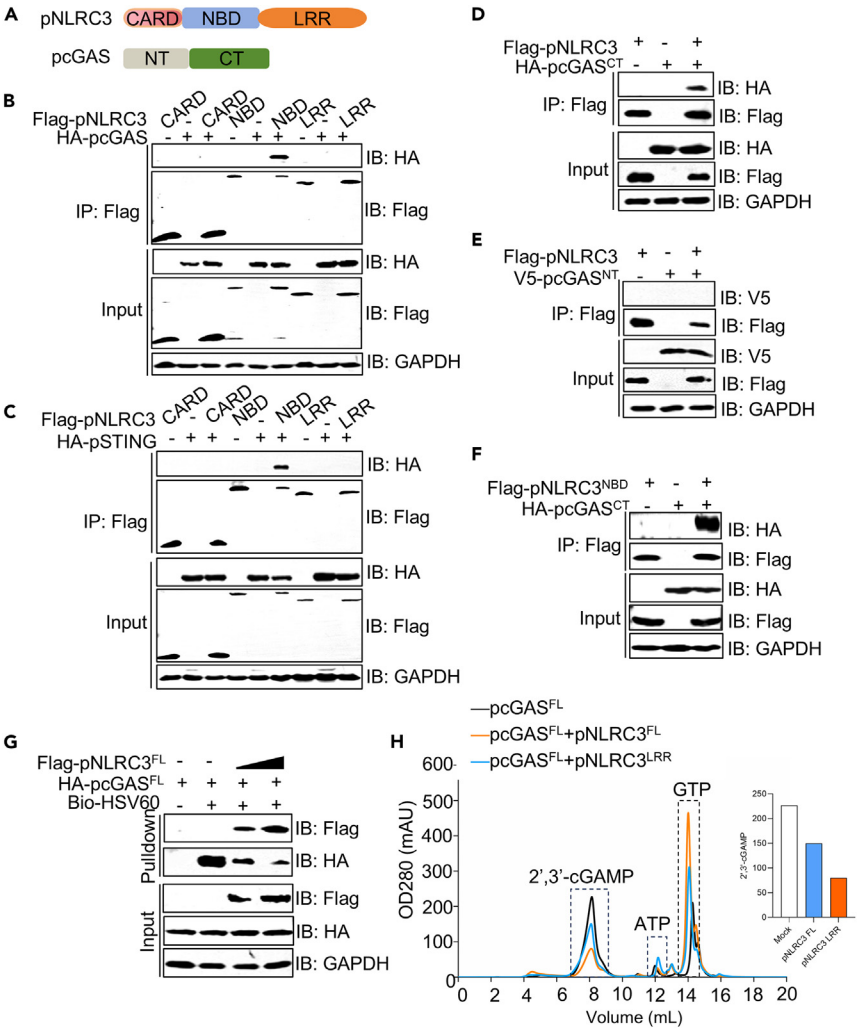

Figure 5. Porcine NLRC3 interferes with DNA binding and attenuates enzymatic function of cGAS

(A) Schematic diagram of pNLRC3 and pcGAS domains.

(B and C) Anti-Flag immunoprecipitates of HA-pcGAS (B) or HA-pSTING (C) with Flag-pNLRC3 mutants in HEK-293T cells. The cell lysates and immunoprecipitates were analyzed by immunoblotting.

(D and E) Anti-Flag immunoprecipitates of HA-pcGAS^{CT} (D) and V5-pcGAS^{NT} (E) with Flag-pNLRC3 in HEK-293T cells.

(F) Anti-Flag immunoprecipitates of HA-pcGAS^{CT} with Flag-pNLRC3^{NBD} in HEK-293T cells.

(G) Streptavidin pull-down assay for the binding of biotin-HSV60 dsDNA to HA-pcGAS in HEK-293T cells. Flag-pNLRC3 was added in a dose as a competitor.

(H) cGAS activity assay by ion-exchange chromatography. 10 μM pcGAS^{FL} was incubated with the Salmon Sperm DNA in reaction buffer at 37°C for 2 h. Analyzing the effects of pNLRC3^{FL} or pNLRC3^{LRR} on cGAMP production using a Mono Q ion-exchange column.

activity. As a control, both hNLRC3 WT and G1032R significantly inhibit pcGAS to produce 2′,3′-cGAMP. The inhibition is likely because hNLRC3 outcompetes cGAS on DNA but not the interaction with cGAS (Figures 6F and S8A).

DISCUSSION

The cytosolic nucleic acids sensors defense the invasion of foreign pathogens through transducing innate immune responses,[28–30] however, the excessive reaction results in immune imbalance, called "cytokine storm". Many literatures reported the excessive inflammatory responses caused the death, such as COVID-19.[31–35] A sub-group of NLRs, including NLRX1, NLRC3, NLRP12, NLRC5, are important proteins to inhibit inflammatory responses as checkpoint,[4,12,36,37] which is similar to programmed cell death-1 (PD-1) and PD-L1. NLRX1 was identified the first inhibitory NLR protein that negatively regulates IFN-I induction. It is an RNA binding protein and binds RNA via its LRR domain.[12] NLRC3 is an intracellular NLR, which negatively regulates multiple innate immune pathways.[20,38–43] We discovered hNLRC3 directly binds to nucleic acids via the LRR with high affinity. Recently, the Hornung group reported that human NLRP1 but not murine NLRP1B binds to dsRNA via LRR with high affinity in a similar manner.[44]

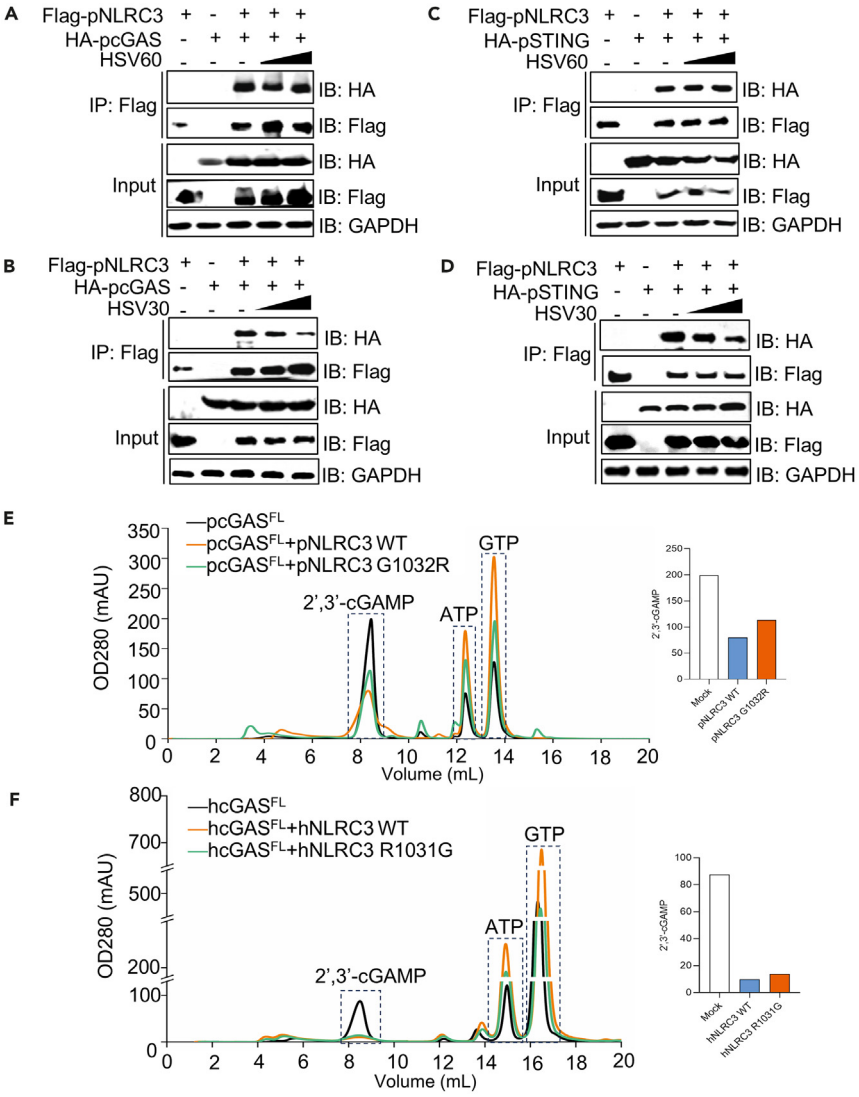

Figure 6. Porcine NLRC3 facilitates the activation of cGAS by binding short dsDNA

(A and B) Anti-Flag immunoprecipitates from HEK-293T cells transfected with Flag-pNLRC3 and HA-pcGAS and increasing HSV60 (A) or HSV30 (B) dsDNA in a dose.

(C and D) Anti-Flag immunoprecipitates from HEK-293T cells transfected with Flag-pNLRC3 and HA-pSTING and increasing HSV60 (C) or HSV30 (D) dsDNA in a dose.

(E) cGAS activity assay was performed with HSV60 to detect the cGAMP level when adding equal pNLRC3 WT or pNLRC3 G1032R lysate from HEK-293T cells. The total proteins were determined by BCA quantitative kit.

(F) cGAS activity assay was performed with HSV60 to detect the cGAMP level when adding equal hNLRC3 WT or hNLRC3 R1031G lysate from HEK-293T cells. The total proteins were determined by BCA quantitative kit.

pNLRC3 binds to viral dsDNA through both its NBD and LRR domains, contrasting hNLRC3, hNLRX1, and hNLRP1, which engage nucleic acids predominantly via the LRR, highlighting distinct dsDNA binding capabilities between pNLRC3 and hNLRC3 variants. Furthermore, we used all-atom MD to simulate the interactions between NLRC3 and various lengths of dsDNA. Interestingly, we found pNLRC3 tended to bind short DNA, whereas hNLRC3 preferred long dsDNA. Previously, we showed that hNLRC3 binds to dsDNA through LRR 1–4 and 13–16 by pull-down and mutagenesis. Here, we reported pNLRC3 binds to dsDNA via LRR 1–4. In addition, we observed the difference in electrostatic surface of LRR 13–16 region between hNLRC3 and pNLRC3 and then aligned the sequences. Interestingly, we observed that hNLRC3 processes an arginine at residue 1031 while this residue is replaced by a glycine residue in pNLRC3, which attracted our attention to determine the biological significance of this replacement. Surprisingly, hNLRC3 R1031G shows a preference for binding to short DNA, in line with the native binding affinity observed in pNLRC3 WT. Conversely, pNLRC3 G1032R prefers to bind to longer DNA, similar to the binding behavior of hNLRC3 WT. There are two binding regions in hNLRC3 LRR, which anchor long dsDNA to form a "bridge". However, pNLRC3 LRR only

processes one end to interact with DNA, explaining why it prefers to bind shorter DNA. It is reported that HSV-1 UL37 tegument protein deamidates a critical Asn on cGAS of humans and mice but not many non-human primates to defines HSV-1 species-specific permissiveness.[45] Therefore, mutation in a single residue in different species may lead to distinction in their innate immune defense and viral evasion.

Since pNLRC3 interacts and inhibits both cGAS and STING, we sought to test whether pNLRC3 could dissociate from cGAS and STING upon binding to DNA in a length-dependent manner. Consistently, pNLRC3 dissociates from cGAS and STING when binding to short DNA but not long DNA. What is the function of short DNA and long DNA in the cytosol? Interestingly, there are a population of small cytosolic dsDNA (scDNA) molecules, which are 20–30 nucleotides (nt) in the human cells were identified as the byproducts of nucleotide excision repair (NER).[25] Recently, scDNA molecules have been reported to repress cGAS activation by competing with long dsDNA and induce autophagy.[25] Hence, we speculated why primates show preference for binding to long DNA while non-primates exhibit preference for binding to short DNA. Primates have evolved the precise recognition to distinguish DNA from self and non-self for avoiding excessive cytokine secretion and autoimmune diseases. hNLRC3 is not easily recognized to short DNA and processes a tight regulation of STING and TBK1 for a high threshold to be activated. However, non-primates, for example, pigs are more sensitive to short DNA (20–40 bp) and unleash the cGAS-STING pathway activation, which may result in immune imbalance. The absence of the AIM2 in the porcine genome piques interest in alternative immune detection mechanism. Further study into the porcine immune response is crucial to understand the evolution of the innate immune responses across species.

Limitations of the study

Despite multiple attempts, we have been unable to obtain large quantities of high-purity recombinant pNLRC3 protein, making it impossible to directly resolve the structure of pNLRC3 complexed with DNA, which hinders our understanding of its precise binding sites. There is also a lack of direct physiological evidence for pNLRC3's role during viral infection, as we do not have endogenous antibodies with high specificity and sensitivity. Although we have identified that pNLRC3 interacts with pcGAS through its NBD domain, the motif of the binding sites remains unknown. These questions need further studies to be resolved.

RESOURCE AVAILABILITY

Lead contact

Further information and requests for resources and reagents should be directed to the lead contact, Xin Li (xinli2021@cau.edu.cn).

Materials availability

This study did not generate new unique reagents.

Data and code availability

- This study did not generate standardized datasets. All data supporting the findings of this study are found within the article and its supplemental information.
- This paper does not report any original code.
- Any additional information required to reanalyze the data reported in this paper is available from the lead contact upon request.

ACKNOWLEDGMENTS

This study was supported by the National Natural Science Foundation of China (32373020) and National Key Research and Development Program of China (2022YFD1800300) to X.L., National Key Research and Development Program of China (2020YFA0908501) and the National Natural Science Foundation of China (22077094) to C.Z., NIH Grant (R01AI145287) and the Welch Foundation grant (A-2107) to P.L. We thank Dr. Yandong Tang (Harbin Veterinary Research Institute) for providing us with PAM-tang cells. The funders had no role in study design, data collection and analysis, decision to publish, or preparation of the manuscript.

AUTHOR CONTRIBUTIONS

Conceptualization: X.L.; data curation: M.L. and C.Z.; methodology: Y.Yuan., X.H., L.W., Y.W., Y.Y., L.C., Y.Q., and Y.Yan.; investigation: M.L. and C.Z.; funding acquisition: X.L. and C.Z.; project administration: X.L.; supervision: X.L.; writing—original draft: X.L., M.L., and C.Z.; writing—review and editing: P.L.

DECLARATION OF INTERESTS

The authors declare no competing interests.

STAR★METHODS

Detailed methods are provided in the online version of this paper and include the following:

- KEY RESOURCES TABLE
- EXPERIMENTAL MODEL AND STUDY PARTICIPANT DETAILS
  - Cell culture
- METHOD DETAILS
  - The UniProt accession ID of NLRC3 gene
  - Plasmids and molecular cloning
  - Plasmids transfection

- DNA and RNA sequences
- Western blot analysis
- Pull-down assay
- Dual-luciferase reporter assay
- Real time RT-PCR
- RNA interference
- Stimulation assay
- Co-immunoprecipitation (Co-IP)
- Confocal microscopy
- Recombinant protein purification and *in vitro* pull-down assay
- Computational modeling
- The MicroScale thermophoresis assay (MST)
- The cGAS activity assay
- Animal silhouettes

● QUANTIFICATION AND STATISTICAL ANALYSIS

SUPPLEMENTAL INFORMATION

Supplemental information can be found online at https://doi.org/10.1016/j.isci.2024.111145.

Received: May 28, 2024
Revised: August 7, 2024
Accepted: October 7, 2024
Published: October 10, 2024

REFERENCES

1. Guo, H., Callaway, J.B., and Ting, J.P.Y. (2015). Inflammasomes: mechanism of action, role in disease, and therapeutics. Nat. Med. *21*, 677–687. https://doi.org/10.1038/nm.3893.
2. Harton, J.A., Linhoff, M.W., Zhang, J., and Ting, J.P.Y. (2002). Cutting Edge: CATERPILLER: A Large Family of Mammalian Genes Containing CARD, Pyrin, Nucleotide-Binding, and Leucine-Rich Repeat Domains. J. Immunol. *169*, 4088–4093. https://doi.org/10.4049/jimmunol.169.8.4088.
3. Barnett, K.C., Li, S., Liang, K., and Ting, J.P.Y. (2023). A 360° view of the inflammasome: Mechanisms of activation, cell death, and diseases. Cell *186*, 2288–2312. https://doi.org/10.1016/j.cell.2023.04.025.
4. Morrison, H.A., Trusiano, B., Rowe, A.J., and Allen, I.C. (2023). Negative regulatory NLRs mitigate inflammation via NF-κB pathway signaling in inflammatory bowel disease. Biomed. J. *46*, 100616. https://doi.org/10.1016/j.bj.2023.100616.
5. Chamaillard, M., Hashimoto, M., Horie, Y., Masumoto, J., Qiu, S., Saab, L., Ogura, Y., Kawasaki, A., Fukase, K., Kusumoto, S., et al. (2003). An essential role for NOD1 in host recognition of bacterial peptidoglycan containing diaminopimelic acid. Nat. Immunol. *4*, 702–707. https://doi.org/10.1038/ni945.
6. Girardin, S.E., Boneca, I.G., Carneiro, L.A.M., Antignac, A., Jéhanno, M., Viala, J., Tedin, K., Taha, M.K., Labigne, A., Zähringer, U., et al. (2003). Nod1 detects a unique muropeptide from gram-negative bacterial peptidoglycan. Science *300*, 1584–1587. https://doi.org/10.1126/science.1084677.
7. Girardin, S.E., Travassos, L.H., Hervé, M., Blanot, D., Boneca, I.G., Philpott, D.J., Sansonetti, P.J., and Mengin-Lecreulx, D. (2003). Peptidoglycan Molecular Requirements Allowing Detection by Nod1 and Nod2. J. Biol. Chem. *278*, 41702–41708. https://doi.org/10.1074/jbc.M307198200.
8. Mo, J., Boyle, J.P., Howard, C.B., Monie, T.P., Davis, B.K., and Duncan, J.A. (2012). Pathogen Sensing by Nucleotide-binding Oligomerization Domain-containing Protein 2 (NOD2) Is Mediated by Direct Binding to Muramyl Dipeptide and ATP. J. Biol. Chem. *287*, 23057–23067. https://doi.org/10.1074/jbc.M112.344283.
9. Hara, H., Seregin, S.S., Yang, D., Fukase, K., Chamaillard, M., Alnemri, E.S., Inohara, N., Chen, G.Y., and Núñez, G. (2018). The NLRP6 Inflammasome Recognizes Lipoteichoic Acid and Regulates Gram-Positive Pathogen Infection. Cell *175*, 1651–1664.e14. https://doi.org/10.1016/j.cell.2018.09.047.
10. Reyes Ruiz, V.M., Ramirez, J., Naseer, N., Palacio, N.M., Siddarthan, I.J., Yan, B.M., Boyer, M.A., Pensinger, D.A., Sauer, J.D., and Shin, S. (2017). Broad detection of bacterial type III secretion system and flagellin proteins by the human NAIP/NLRC4 inflammasome. Proc. Natl. Acad. Sci. USA *114*, 13242–13247. https://doi.org/10.1073/pnas.1710433114.
11. Moore, C.B., Bergstralh, D.T., Duncan, J.A., Lei, Y., Morrison, T.E., Zimmermann, A.G., Accavitti-Loper, M.A., Madden, V.J., Sun, L., Ye, Z., et al. (2008). NLRX1 is a regulator of mitochondrial antiviral immunity. Nature *451*, 573–577. https://doi.org/10.1038/nature06501.
12. Hong, M., Yoon, S.I., and Wilson, I.A. (2012). Structure and functional characterization of the RNA-binding element of the NLRX1 innate immune modulator. Immunity *36*, 337–347. https://doi.org/10.1016/j.immuni.2011.12.018.
13. Kato, H., Takeuchi, O., Mikamo-Satoh, E., Hirai, R., Kawai, T., Matsushita, K., Hiiragi, A., Dermody, T.S., Fujita, T., and Akira, S. (2008). Length-dependent recognition of double-stranded ribonucleic acids by retinoic acid-inducible gene- I and melanoma differentiation-associated gene 5. J. Exp. Med. *205*, 1601–1610. https://doi.org/10.1084/jem.20080091.
14. Peisley, A., Lin, C., Wu, B., Orme-Johnson, M., Liu, M., Walz, T., and Hur, S. (2011). Cooperative assembly and dynamic disassembly of MDA5 filaments for viral dsRNA recognition. Proc. Natl. Acad. Sci. USA *108*, 21010–21015. https://doi.org/10.1073/pnas.1113651108.
15. Morrone, S.R., Matyszewski, M., Yu, X., Delannoy, M., Egelman, E.H., and Sohn, J. (2015). Assembly-driven activation of the AIM2 foreign-dsDNA sensor provides a polymerization template for downstream ASC. Nat. Commun. *6*, 7827. https://doi.org/10.1038/ncomms8827.
16. Morrone, S.R., Wang, T., Constantoulakis, L.M., Hooy, R.M., Delannoy, M.J., and Sohn, J. (2013). Cooperative assembly of IFI16 filaments on dsDNA provides insights into host defense strategy. Proc. Natl. Acad. Sci. USA *111*. E62-71. https://doi.org/10.1073/pnas.1313577111.
17. Andreeva, L., Hiller, B., Kostrewa, D., Lässig, C., de Oliveira Mann, C.C., Jan Drexler, D., Maiser, A., Gaidt, M., Leonhardt, H., Hornung, V., and Hopfner, K.P. (2017). cGAS senses long and HMGB/TFAM-bound U-turn DNA by forming protein–DNA ladders. Nature *549*, 394–398. https://doi.org/10.1038/nature23890.
18. Li, X., Shu, C., Yi, G., Chaton, C.T., Shelton, C.L., Diao, J., Zuo, X., Kao, C.C., Herr, A.B., and Li, P. (2013). Cyclic GMP-AMP Synthase Is Activated by Double-Stranded DNA-Induced Oligomerization. Immunity *39*, 1019–1031. https://doi.org/10.1016/j.immuni.2013.10.019.
19. Schneider, M., Zimmermann, A.G., Roberts, R.A., Zhang, L., Swanson, K.V., Wen, H., Davis, B.K., Allen, I.C., Holl, E.K., Ye, Z., et al. (2012). The innate immune sensor NLRC3 attenuates Toll-like receptor signaling via modification of the signaling adaptor TRAF6 and transcription factor NF-κB. Nat. Immunol. *13*, 823–831. https://doi.org/10.1038/ni.2378.
20. Xu, J., Gao, C., He, Y., Fang, X., Sun, D., Peng, Z., Xiao, H., Sun, M., Zhang, P., Zhou, T., et al. (2023). NLRC3 expression in macrophage impairs glycolysis and host immune defense by modulating the NF-κB-NFAT5 complex during septic immunosuppression. Mol. Ther. *31*, 154–173. https://doi.org/10.1016/j.ymthe.2022.08.023.

21. Zhang, L., Mo, J., Swanson, K.V., Wen, H., Petrucelli, A., Gregory, S.M., Zhang, Z., Schneider, M., Jiang, Y., Fitzgerald, K.A., et al. (2014). NLRC3, a Member of the NLR Family of Proteins, Is a Negative Regulator of Innate Immune Signaling Induced by the DNA Sensor STING. Immunity *40*, 329–341. https://doi.org/10.1016/j.immuni.2014.01.010.
22. Karki, R., Man, S.M., Malireddi, R.K.S., Kesavardhana, S., Zhu, Q., Burton, A.R., Sharma, B.R., Qi, X., Pelletier, S., Vogel, P., et al. (2016). NLRC3 is an inhibitory sensor of PI3K–mTOR pathways in cancer. Nature *540*, 583–587. https://doi.org/10.1038/nature20597.
23. Li, X., Deng, M., Petrucelli, A.S., Zhu, C., Mo, J., Zhang, L., Tam, J.W., Ariel, P., Zhao, B., Zhang, S., et al. (2019). Viral DNA Binding to NLRC3, an Inhibitory Nucleic Acid Sensor, Unleashes STING, a Cyclic Dinucleotide Receptor that Activates Type I Interferon. Immunity *50*, 591–599.e6. https://doi.org/10.1016/j.immuni.2019.02.009.
24. Luecke, S., Holleufer, A., Christensen, M.H., Jønsson, K.L., Boni, G.A., Sørensen, L.K., Johannsen, M., Jakobsen, M.R., Hartmann, R., and Paludan, S.R. (2017). cGAS is activated by DNA in a length-dependent manner. EMBO Rep. *18*, 1707–1715. https://doi.org/10.15252/embr.201744017.
25. Liu, Y., Chen, X., Zhao, Y., Wang, X.-Y., Luo, Y.-W., Chen, L., Wang, W., Zhong, S., Hu, M., Dai, Z., et al. (2023). Small cytosolic double-stranded DNA represses cyclic GMP-AMP synthase activation and induces autophagy. Cell Rep. *42*, 112852. https://doi.org/10.1016/j.celrep.2023.112852.
26. Zhou, W., Whiteley, A.T., and Kranzusch, P.J. (2019). Analysis of human cGAS activity and structure. Methods Enzymol. *625*, 13–40.
27. Yan, Y., Wu, L., Yuan, Y., Wang, H., Yin, H., Li, M., Chai, L., Liang, R., Liu, Y., Zhao, D., et al. (2023). Species-specific cleavage of cGAS by picornavirus protease 3C disrupts mitochondria DNA-mediated immune sensing. PLoS Pathog. *19*, e1011641. https://doi.org/10.1371/journal.ppat.1011641.
28. Mosallanejad, K., Kennedy, S.N., Bahleda, K.M., Slavik, K.M., Zhou, W., Govande, A.A., Hancks, D.C., Kranzusch, P.J., and Kagan, J.C. (2023). Species-specific self- DNA detection mechanisms by mammalian cyclic GMP-AMP synthases. Sci. Immunol. *8*, eabp9765. https://doi.org/10.1126/sciimmunol.abp9765.
29. Fu, J., Schroder, K., and Wu, H. (2024). Mechanistic insights from inflammasome structures. Nat. Rev. Immunol. *24*, 518–535. https://doi.org/10.1038/s41577-024-00995-w.
30. Schlee, M., and Hartmann, G. (2016). Discriminating self from non-self in nucleic acid sensing. Nat. Rev. Immunol. *16*, 566–580. https://doi.org/10.1038/nri.2016.78.
31. Diamond, M.S., and Kanneganti, T.D. (2022). Innate immunity: the first line of defense against SARS-CoV-2. Nat. Immunol. *23*, 165–176. https://doi.org/10.1038/s41590-021-01091-0.
32. Junqueira, C., Crespo, Â., Ranjbar, S., de Lacerda, L.B., Lewandrowski, M., Ingber, J., Parry, B., Ravid, S., Clark, S., Schrimpf, M.R., et al. (2022). FcγR-mediated SARS-CoV-2 infection of monocytes activates inflammation. Nature *606*, 576–584. https://doi.org/10.1038/s41586-022-04702-4.
33. Pan, P., Shen, M., Yu, Z., Ge, W., Chen, K., Tian, M., Xiao, F., Wang, Z., Wang, J., Jia, Y., et al. (2021). SARS-CoV-2 N protein promotes NLRP3 inflammasome activation to induce hyperinflammation. Nat. Commun. *12*, 4664. https://doi.org/10.1038/s41467-021-25015-6.
34. Song, J., Li, K., Li, T., Zhao, G., Zhou, S., Li, H., Li, J., and Weng, C. (2020). Screening of PRRSV- and ASFV-encoded proteins involved in the inflammatory response using a porcine iGLuc reporter. J. Virol. Methods *285*, 113958. https://doi.org/10.1016/j.jviromet.2020.113958.
35. Zhang, K., Hou, Q., Zhong, Z., Li, X., Chen, H., Li, W., Wen, J., Wang, L., Liu, W., and Zhong, F. (2013). Porcine reproductive and respiratory syndrome virus activates inflammasomes of porcine alveolar macrophages via its small envelope protein E. Virology *442*, 156–162. https://doi.org/10.1016/j.virol.2013.04.007.
36. Ye, Z., Lich, J.D., Moore, C.B., Duncan, J.A., Williams, K.L., and Ting, J.P.Y. (2008). ATP Binding by Monarch-1/NLRP12 Is Critical for Its Inhibitory Function. Mol. Cell Biol. *28*, 1841–1850. https://doi.org/10.1128/mcb.01468-07.
37. Wu, Y., Shi, T., and Li, J. (2019). NLRC5: A paradigm for NLRs in immunological and inflammatory reaction. Cancer Lett. *451*, 92–99. https://doi.org/10.1016/j.canlet.2019.03.005.
38. Conti, B.J., Davis, B.K., Zhang, J., O'Connor, W., Williams, K.L., and Ting, J.P.Y. (2005). CATERPILLER 16.2 (CLR16.2), a Novel NBD/LRR Family Member That Negatively Regulates T Cell Function. J. Biol. Chem. *280*, 18375–18385. https://doi.org/10.1074/jbc.M413169200.
39. Eren, E., Berber, M., and Özören, N. (2017). NLRC3 protein inhibits inflammation by disrupting NALP3 inflammasome assembly via competition with the adaptor protein ASC for pro-caspase-1 binding. J. Biol. Chem. *292*, 12691–12701. https://doi.org/10.1074/jbc.M116.769695.
40. Hu, S., Du, X., Huang, Y., Fu, Y., Yang, Y., Zhan, X., He, W., Wen, Q., Zhou, X., Zhou, C., et al. (2018). NLRC3 negatively regulates CD4+ T cells and impacts protective immunity during Mycobacterium tuberculosis infection. PLoS Pathog. *14*, e1007266. https://doi.org/10.1371/journal.ppat.1007266.
41. Niu, L., Luo, G., Liang, R., Qiu, C., Yang, J., Xie, L., Zhang, K., Tian, Y., Wang, D., Song, S., et al. (2022). Negative Regulator Nlrc3-like Maintain the Balanced Innate Immune Response During Mycobacterial Infection in Zebrafish. Front. Immunol. *13*, 893611. https://doi.org/10.3389/fimmu.2022.893611.
42. Qin, Y., Wu, K., Zhang, Z., Pan, R., Lin, Z., Zhang, W., Huang, S., Dai, J., Huang, R., Gong, S., et al. (2022). NLRC3 deficiency promotes cutaneous wound healing due to the inhibition of p53 signaling. Biochim. Biophys. Acta, Mol. Basis Dis. *1868*, 166518. https://doi.org/10.1016/j.bbadis.2022.166518.
43. Sun, D., Xu, J., Zhang, W., Song, C., Gao, C., He, Y., and Shang, Y. (2022). Negative regulator NLRC3: Its potential role and regulatory mechanism in immune response and immune-related diseases. Front. Immunol. *13*, 1012459. https://doi.org/10.3389/fimmu.2022.1012459.
44. Bauernfried, S., Scherr, M.J., Pichlmair, A., Duderstadt, K.E., and Hornung, V. (2021). Human NLRP1 is a sensor for double-stranded RNA. Science *371*, eabd0811. https://doi.org/10.1126/science.abd0811.
45. Zhang, J., Zhao, J., Xu, S., Li, J., He, S., Zeng, Y., Xie, L., Xie, N., Liu, T., Lee, K., et al. (2018). Species-Specific Deamidation of cGAS by Herpes Simplex Virus UL37 Protein Facilitates Viral Replication. Cell Host Microbe *24*, 234–248.e5. https://doi.org/10.1016/j.chom.2018.07.004.
46. Wang, T.Y., Liu, Y.G., Li, L., Wang, G., Wang, H.M., Zhang, H.L., Zhao, S.F., Gao, J.C., An, T.Q., Tian, Z.J., et al. (2018). Porcine alveolar macrophage CD163 abundance is a pivotal switch for porcine reproductive and respiratory syndrome virus infection. Oncotarget *9*, 12174–12185. https://doi.org/10.18632/oncotarget.24040.
47. Huang, J., and MacKerell, A.D., Jr. (2013). CHARMM36 all-atom additive protein force field: validation based on comparison to NMR data. J. Comput. Chem. *34*, 2135–2145. https://doi.org/10.1002/jcc.23354.
48. Páll, S., Zhmurov, A., Bauer, P., Abraham, M., Lundborg, M., Gray, A., Hess, B., and Lindahl, E. (2020). Heterogeneous parallelization and acceleration of molecular dynamics simulations in GROMACS. J. Chem. Phys. *153*, 134110. https://doi.org/10.1063/5.0018516.
49. Varadi, M., Anyango, S., Deshpande, M., Nair, S., Natassia, C., Yordanova, G., Yuan, D., Stroe, O., Wood, G., Laydon, A., et al. (2022). AlphaFold Protein Structure Database: massively expanding the structural coverage of protein-sequence space with high-accuracy models. Nucleic Acids Res. *50*. D439-d444. https://doi.org/10.1093/nar/gkab1061.

STAR★METHODS

KEY RESOURCES TABLE

REAGENT or RESOURCE	SOURCE	IDENTIFIER
Antibodies		
Mouse anti-Flag	Sigma-Aldrich	Cat# F1804; RRID: AB_262044
Rabbit anti-HA	Cell Signaling Technology	Cat# 3724; RRID: AB_1549585
Rabbit anti-V5	Cell Signaling Technology	Cat# 13202; RRID: AB_2153491
Mouse anti-His	GeneScript	Cat# A00186-100; RRID: AB_914704
Rabbit anti-Strep-II	Abcom	Cat# ab76950; RRID: AB_1524456
GAPDH Rabbit Polyclonal antibody	Proteintech	Cat# 10494-1-AP; RRID: AB_2263076
Anti-mouse IgG HRP-Linked Antibody	Cell Signaling Technology	Cat# 7076; RRID: AB_330924
Anti-rabbit IgG HRP-Linked Antibody	Cell Signaling Technology	Cat# 7074; RRID: AB_2099233
ALexa Flour 633 goat anti-mouse IgG(H + L)	Invitrogen	Cat# A21052; RRID: AB_2535719
ALexa Flour 488 goat anti-Rabbit IgG(H + L)	Invitrogen	Cat# A11034; RRID: AB_2576217
Bacterial strains		
BL21	Tsingke Biotech	Cat# CD601
DH5α	Vazyme	Cat# C502-02
Plasmids		
pcDNA3.1-HA/Flag-pNLRC3	This paper	N/A
pcDNA3.1-GFP-pNLRC3-8xHis	This paper	N/A
pcDNA3.1-HA-pNLRC3 G1032R	This paper	N/A
pcDNA3.1-HA/Flag-pNLRC3 CARD	This paper	N/A
pcDNA3.1-HA/Flag-pNLRC3 CARD-NBD	This paper	N/A
pcDNA3.1-HA/Flag-pNLRC3 NBD	This paper	N/A
pcDNA3.1-HA/Flag-pNLRC3 NBD-LRR	This paper	N/A
pcDNA3.1-HA/Flag-pNLRC3 LRR	This paper	N/A
pcDNA3.1-HA-pcGAS	This paper	N/A
pcDNA3.1-HA-pSTING	This paper	N/A
pcDNA3.1-HA-pTBK1	This paper	N/A
pcDNA3.1-HA-pIRF3	This paper	N/A
pcDNA3.1-HA/Flag-hNLRC3	This paper	N/A
pcDNA3.1-HA-hNLRC3 R1031G	This paper	N/A
pcDNA3.1-HA-hcGAS	This paper	N/A
pcDNA3.1-HA-hSTING	This paper	N/A
pcDNA3.1-HA-hTBK1	This paper	N/A
pcDNA3.1-HA-hIRF3	This paper	N/A
pcDNA3.1-HA-hRIG-I	This paper	N/A
PiggyBac-EGFP-Strep-II-pNLRC3	This paper	N/A
pGEX-4T-1-GST-pNLRC3 NBD	This paper	N/A
pET28a-His-pNLRC3 LRR	This paper	N/A
pET28a-His-pcGAS	This paper	N/A
Chemicals		
DMEM	Macgene	Cat# CM10013
RPMI medium 1640	Macgene	Cat# C11875500CP

(*Continued on next page*)

Continued

REAGENT or RESOURCE	SOURCE	IDENTIFIER
PBS	Macgene	Cat# P1020
Fetal Bovine Serum	CellMax	Cat# SA211.02
Puromycin	Solarbio	Cat# P8230
Fixative solution	Solarbio	Cat# P1110
NP-40	Solarbio	Cat# N8032
Isopropyl β-D-1-thiogalactoside	Solarbio	Cat# 18070
Mycoplasma OUT	Genloci	Cat# 24010301
Opti-MEM	Gibco	Cat# 31985070
Lipofectamine2000	Invitrogen	Cat# 11668019
RNAiMAX	Invitrogen	Cat# 13778150
Lipofectamine8000	Beyotime	Cat# C0533-0.5mL
DAPI	Beyotime	Cat# C1002
Cell lysis buffer for Western and IP	Beyotime	Cat# P0013J
PVDF	Millipore	Cat# ISEQ00010
cOmplete™ Protease Inhibitor Cocktails	Roche	Cat# 5892970001
Serum-Free Cell Freezing Medium	NCM	Cat# C40100
DMSO	Sigma	Cat# D2650
Bovine serum albumin	Sigma	Cat# A7906-100G
poly(dA:dT)	Invitrogen	Cat# tlrl-patn
2′,3′-cGAMP	Invitrogen	Cat# tlrl-nacga23
Prestained Protein Ladder	Thermo Scientific	Cat# 26616
SuperSignal™ West Pico PLUS	Thermo Scientific	Cat# 34578
Strep-Tactin®XT 4Flow® high capacity column	IBA Lifesciences	Cat# 2-5032-001
Streptavidin MagPoly beads	Smart-Lifesciences	Cat# SM017010
D-Biotin	Smart-Lifesciences	Cat# SLR00602
Protein A/G	Santa cruz	Cat# sc-2003
HiloadTM 16/600 SuperdexTM 200 pg	Cytiva	Cat# 28989335
Mono Q ion-exchange column	Cytiva	Cat# 17516601
Stripping Buffer	CWBIO	Cat# CW0056M
DL500 DNA Marker	TaKaRa	Cat# 3590A
DL1000 DNA Marker	TaKaRa	Cat# 3591A
DL2000 DNA Marker	TaKaRa	Cat# 3428A
DL5000 DNA Marker	TaKaRa	Cat# 3427A
Primestar	TaKaRa	Cat# R045A
T4 DNA Ligase	TaKaRa	Cat# 2011A
2×Taq Master Mix	Vazyme	Cat# P112-01
HiScript II Q RT SuperMix	Vazyme	Cat# R223-01
Taq Pro Universal SYBR Qpcr Master Mix	Vazyme	Cat# Q712-02
Ni-NTA resin	QIAGEN	Cat# 30230
Glutathione Resin	GeneScript	Cat# L00206
Critical commercial assays		
BCA protein assay kit	Solarbio	Cat# PC0020
ClonExpress II One Step Cloning Kit	Vazyme	Cat# C112-02
Mut Express® II Fast Mutagenesis Kit	Vazyme	Cat# C214
Qiaquick PCR purification kit	QIAGEN	Cat# 28104

(*Continued on next page*)

Continued

REAGENT or RESOURCE	SOURCE	IDENTIFIER
RNA simple total RNA extraction kit	TIANGEN	Cat# DP419
Dual-Luciferase Reporter Assay System kit	Promega	Cat# E1960
Experimental models: Cell lines		
HEK-293T	This paper	N/A
Immortalized PAM cells (PAM-Tang)	Harbin Veterinary Research Institute	N/A
PK-15	This paper	N/A
HeLa	This paper	N/A
Oligonucleotides		
HT-DNA	Thermo Scientific	Cat# 15632011
Biotin-HSV120	This paper	N/A
Biotin-HSV60	This paper	N/A
Biotin-HSV30	This paper	N/A
Biotin-HSV15	This paper	N/A
HSV120	This paper	N/A
HSV60	This paper	N/A
HSV30	This paper	N/A
Software and algorithms		
Graphpad Prism 8	GraphPad Software	https://www.graphpad.com/
MO. Affinity Analysis	MO. Affinity Analysis software	https://www.bioz.com/

EXPERIMENTAL MODEL AND STUDY PARTICIPANT DETAILS

Cell culture

HEK-293T cells (Human embryonic kidney cells), PK-15 cells (Porcine kidney-15) and HeLa cells were cultured in Dulbecco's Modified Eagle Medium (DMEM) (MACGENE, #CM10013) containing 10% fetal bovine serum (FBS) (CellMax, #SA211.02), 100 μg/mL streptomycin, 1% penicillin. Immortalized PAMs (PAM-Tang) were provided by Dr. Yandong. Tang (Harbin veterinary research institute of Chinese Academy of Agricultural Sciences (CAAS), Harbin, China)[46] and maintained in RPMI medium 1640 (MACGENE, #C11875500CP) supplemented with 10% FBS, 100 μg/mL streptomycin, 1% penicillin. HEK-293T cell line stably expressing Strep-II-pNLRC3 was constructed using PiggyBac Transposon system and detected by the microscope (Falcon S400, Alicelligent Technologies). All cells were grown at 37°C incubator under 5% CO_2.

METHOD DETAILS

The UniProt accession ID of NLRC3 gene

All sequences of NLRC3 in different species are from UniProt. Human (Q7RTR2), black snub-nosed monkey (A0A2K6MM34), Golden monkey (A0A2K6MM34), Sapajou (A0A6J3G830), Green monkey (A0A0D9RC41), Ma's night monkey (A0A2K5D8M7), Cynomolgus monkey (A0A2K5VQA3), Pig-tailed macaque (A0A2K5VQA3), White-cheeked gibbon (G1REY0), Chinese tree shrew (L9LB10), Olive baboon (A0A096NLC5), Sumatran orangutan (H2NPZ4), Chimpanzee (H2QAG9), Pig (A0A287AW79), Deer (A0A6J0ZAC0), Goat (A0A452FN27), Panda (G1LVY7), Lion (A0A8C8WRG8), Mouse (Q5DU56), Sewer rat (D3ZYP9), Duck (A0A493U1Q4), Chicken (A0A8F2F4X1), Zebrafish (A0A8M3APF3), Drosophila melanogaster (Q7YWY1) and Elegans (A0A0A1XNV3).

Plasmids and molecular cloning

The cDNA of porcine spleen or THP-1 cells were amplificated via polymerase chain reaction (PCR) with specific primers, then the products were cloned into pcDNA3.1 vector by Primestar (TaKaRa, #R045A) and ClonExpressII One Step Cloning Kit (Vezyme, #C112-02). pNLRC3 G1032R and hNLRC3 R1031G mutants were engineered into pcDNA3.1 using Mut Express II Fast Mutagenesis Kit V2 (Vazyme, #C214) according to the manufacturer's instructions. Construction results were confirmed by DNA sequencing (Tsingke, Beijing, China).

Plasmids transfection

HEK-293T cells were seeded in 24-well plates culturing for overnight. The successfully constructed plasmids were mixed with lipofectamine2000 reagent (Invitrogen, #11668019), incubated at room temperature for 15 min, then added to the cells. Six hours later, the supernatant was removed and the cells were incubated in DMEM containing 10% FBS for 24 h. Proteins expressing were confirmed by western blot.

DNA and RNA sequences

15 bp DNA: 5′-biotin-TAAGACACGATGCGA-3′; 30 bp DNA: 5′-biotin-TAAGACACGATGCG ATAAAATCTGTTTGTA; HSV60 bp DNA: 5′-biotin-TAAGACACGATGCGATAAAATCTGTTTGTAAAATTTATTAAGGGTACAAATT-GCCCTAGC-3′; 120 bp DNA: 5′-biotin-TAAGAC ACGATGCGATAAAATCTGTTTGTAAAATTTATTAAGGGTACAAATGCCCTAGCTAGACACGATGCGATAAAATCTGTTTGTAAAATTTATTA AGGGTACAAATTGCCCTAGC-3′; 60 bp RNA: 5′-biotin UAAGACACGAUGCGAUAAAAUCUGUUUGUAAAAUUUAUUAAGGGUACAAAU-UGCCCUAGC-3′; 15 bp RNA: 5′-biotin-UAAGACACGAUGCGA-3′; All biotinylated nucleic acids were synthesized by Sangon Biotech (Shanghai, China)

Western blot analysis

Cells were lysed with Western and IP lysis buffer (Beyotime, #P0013J) supplemented with phosphatase and protease inhibitor cocktail (Roche, #5892970001). The total protein concentrations were detected using a Bicinchoninic Acid (BCA) Protein Assay Kit (Solarbio, #PC0020). The same amount of the extract was treated with SDS buffer separated by SDS-PAGE, and transferred onto polyvinylidene fluoride (PVDF) membranes (Millipore, #ISEQ00010) for immunoblot analysis. Values were normalized to glyceraldehyde-3-phosphate dehydrogenase (GAPDH).

Pull-down assay

HEK-293T cells were cultured in 6-well plates and transfected with indicated plasmids. After 24 h of transfection, HEK-293T cells were washed twice with PBS, collected and lysed with Western and IP buffer supplemented with protease inhibitor cocktail for 30 min. Cell lysate was harvested by centrifugation at 12,000 rpm for 10 min at 4°C, and incubated with biotinylated nucleic acids (synthesized by Sangon Biotech, Shanghai, China) for 4 h at 4°C. Then the mixture containing protein and biotinylated nucleic acids were incubated with streptavidin magnetic beads (Changzhou Smart-Lifesciences Biotechnology, # SM017010) for another 2 h. After washing fives times, the beads were denatured with SDS buffer at 95°C for 10 min and subjected to western blot analysis.

Dual-luciferase reporter assay

HEK-293T cells were cultured in 24-well plates overnight. pRL-TK (30 ng), pGL3.0-IFN-β-Luc (300 ng), pcGAS (200 ng), pSTING (100 ng), or pTBK1 (500 ng), pIRF3 (500 ng) and pNLRC3 (500 ng) plasmids were co-transfected using lipofectamine8000 (Beyotime, #C0533). Samples were harvested at 24 h post-transfection and lysed with 1×passive lysis buffer. The supernatant was collected after centrifugation at 4°C for 10 min, and added to 96-well plates. Then the activities of firefly and renilla luciferase were measured according to the Dual-Luciferase Reporter Assay System (Promega, #E1960).

Real time RT-PCR

Total RNA was extracted by RNA simple Total RNA extraction kit (TIANGEN, #DP419) and was reversely transcribed to cDNA using HiScriptII Q RT SuperMix (Vazyme, #R223-01) according to the manufacturer's protocol. Real-time PCR was performed using 2×Taq Pro Universal SYBR qPCR Master Mix (Vazyme, #Q712-02) on a LightCycler480II system (Roche, Switzerland) in triplicated determinants. The cycle threshold (ΔΔCT) method was used to analyze the target gene expression levels. Data were normalized to GAPDH expression.

Primers used: pIFN-β:

5′-AGTTGCCTGGGACTCCTCAA-3′, 5′-CCTCAGGGACCTCAAAGTTCAT-3′; pGAPDH: 5′-ACATGGCCTCCAAGGAGTAAGA-3′, 5′-GA TCGAGTTGGGGCTGTGACT-3′; pNLRC3: 5′-GGTCAACTCAAGCCTCCGAA-3′, 5′-CAGGACCGGTGGAATTGGAA-3′;

hIFN-β: 5′-CCAACAAGTGTCTCCTCCAAAT-3′,

5′-AATCTCCTCAGGGATGTCAAAGT-3′;

hGAPDH: 5′-CTCTGCTCCTCCTGTTCGAC-3′,

5′-AATCCGTTGACTCC GACCTT-3′

RNA interference

PK-15 and PAM-Tang cells were transfected with small interfering RNA (siRNA) synthesized by GenePharma (Suzhou, China) when the density of cells reached 60% by RNAiMAX transfection reagent (Invitrogen, #13778150) according to the manufacturer's protocol. After 36 h, cells were stimulated with 1 mg/mL of poly(dA:dT) (Invivogen, #tlrl-patn) or 2′,3′-cGAMP (Invivogen, #tlrl-nacga23). The IFN-β mRNA level was detected by RT-qPCR.

Stimulation assay

PK-15, PAM-Tang and HeLa cells were plated in 24-well plates and grown to 80% confluence overnight. The cells were transfected with pNLRC3 using lipofectamine8000 (Beyotime, #C0533) or siRNA of pNLRC3 using RNAiMAX transfection reagent. Transfection of poly(dA:dT) or 2′,3′-cGAMP at 1 μg/mL using lipofectamine 8000 were followed after 24 h post-transfection.

Co-immunoprecipitation (Co-IP)

HEK-293T cells cultured in 6-well plates were transfected with the indicated plasmids by using lipofectamine8000. 24 h post-transfection, cells were collected and lysed with NP-40 (Solarbio, #N8032). After centrifugation for 10 min at 12,000 rpm, supernatant was immunoprecipitated

with mouse anti-Flag monoclonal antibody (Sigma Aldrich, #F1804) and protein A/G plus-agarose (Santa Cruz Bio-technology, #sc-2003). After 6 h of incubation, beads were washed three times with ice-clod PBS. Immunoprecipitates or whole cell lysates were boiled with SDS sample buffer, separated by SDS-PAGE, transferred onto PVDF membranes, and then blotted with specific antibodies.

Confocal microscopy

HEK-293T cells were seeded onto glass coverslips in 24-well plates. When cell density reached up to 40–50%, the cells were co-transfected with Flag-pNLRC3 and HA-pcGAS, HA-pSTING, HA-pIRF3 or Flag-pTBK1 and HA-pNLRC3 plasmids. After 24 h, the cells were washed with PBS, treated with 4% fixative solution (Solarbio, #P1110) for 30 min and permeabilized with 0.1% Triton X-100 for 10 min at room temperature. Then the cells were washed and blocked in 1% bovine serum albumin (Sigma Aldrich, #A7906-100G) at 4°C for 30 min. Subsequently, the cells were incubated with primary antibodies (mouse anti-Flag (Sigma Aldrich, #F1804) and rabbit anti-HA (Cell Signaling Technology, #13202)) for 2 h at 37°C, washed four times with PBS, then stained with secondary antibodies (Alexa Flour 633 goat anti-mouse IgG (H + L) (Invitrogen, #A21052) and Alexa Flour 488 goat anti-rabbit IgG (H + L) (Invitrogen, #A11034)) for 30 min, and the nuclei were treated with DAPI (Beyotime, #C1002) for 5 min. After washing with PBS, the stained cells were analyzed using Falcon S300, Intelligent cell imaging and analysis system (Alicelligent Technologies).

Recombinant protein purification and *in vitro* pull-down assay

For expression and purification of the full-length pNLRC3 recombinant protein, N-terminal Strep-II-tagged pNLRC3 was cloned into PiggyBac vector. Strep-II-pNLRC3-HEK-293T stable expression cell line was constructed by co-transfection PiggyBac-Strep-II-pNLRC3 plasmid and Super PiggyBac Transposase. HEK-293T cell line was washed three times with cold PBS when grown to 100% confluence and lysed with NP-40 for 1 h at 4°C. Samples were centrifuged at 12,000 rpm for 10 min to isolate the supernatant containing full-length pNLRC3 protein. The supernatant was filtered in advance with a 0.45 filter to remove any aggregates that may have formed, then was incubated with 2 mL column bed volume (CV) Strep-TactinXT resins (IBA Lifesciences, #2-5032-001) pre-equilibrated with buffer W (100 mM Tris pH 8.0, 1 mM EDTA, 150 mM NaCl). The supernatant was outflowed and resins were washed with 5 × 1 CV of Buffer W. The full-length pNLRC3 proteins were finally eluted with 6 × 0.5 CV of Buffer BXT (100 mM Tris/HCl, pH 8.0, 1mM EDTA, 150 mM NaCl, 50 mM biotin). GFP-pNLRC3-8×His was cloned into pcDNA3.1 vector, which transfected into HEK-293T cell to purify GFP-pNLRC3 recombinant proteins by Ni-NTA resin (QIAGEN, #30230). pNLRC3 NBD was cloned into pGEX-4T-1 vector with N-terminal GST tag and pNLRC3 LRR was cloned into pET-28(a) vector with N-terminal 6×His-SUMO tag. Successful clones were transformed into *E. coli* BL21(DE3) (Tsingke Biotech, #CD601). The bacteria were cultured at 37°C and the protein expressing was induced by 1 mM isopropyl β-D-1-thiogalactoside (Solarbio, #18070) at 16°C when OD600 arrived at 1.0. The bacteria were harvested and lysed with buffer containing 50 mM Tris-HCl (pH 8.0), 300 mM NaCl. The pNLRC3 NBD supernatant was applied to Glutathione resin (GeneScript, #L00206). The proteins were washed with 10 mM Glutathione elution buffer (L-Glutathione is soluble in 50 mM Tris-HCl (pH 8.0)). The pNLRC3 LRR supernatant was applied to Ni-NTA resin. The proteins were washed with buffer containing 500 mM NaCl, 20 mM Tris-HCl (pH 7.5) and 25 mM imidazole, and eluted in 150 mM, NaCl 20 mM Tris-HCl (pH 7.5), and 250 mM imidazole. Subsequently, the pNLRC3 LRR proteins were further purified with running buffer (150 mM NaCl, 20 mM Tris-HCl (pH 7.5)) using HiloadTM 16/600 SuperdexTM 200 pg (Cytiva, #28989335) gel filtration chromatography. The pcGAS^{FL} recombinant proteins were purified by Ni-NTA beads, Hiload 16/600 Superdex 200pg gel filtration chromatography and resource S ion exchange according to Yan et al.[27] Finally, all proteins were concentrated by ultrafiltration and the concentration was determined by Bradford assay. Purified proteins were frozen in liquid nitrogen and stored in running buffer containing 5 mM DTT.

Computational modeling

The all-atom MD simulations of pNLRC3 and DNA chains (HSV15 and HSV60) were performed on Gromacs 2019.6 with CHARMM36 force field and explicit solvent model TIP3P for waters.[47,48] The structural model of pNLRC3 was downloaded from the AlphaFold Protein Structure Database with the UniProt accession ID A0A287AW7.[49] The structural models of double strands DNA were adapted from the previous study.[23] Throughout the simulations, no constraints were implemented on neither protein chains nor DNA chains. The initial poses of the NLRC3-DNA complex were adapted from the productive trajectories of simulations on hNLRC3 and the 15 bp/60 bp dsDNA chains were close to the LRR domain. The system (63 136–226 805 atoms) was embedded in a water box (115 × 115 × 110 Å^3 for 15 bp and 187 × 187 × 187 Å^3 for 60 bp) neutralized with 150 mM NaCl, minimized using steepest descent method before equilibration of 10 ns at 303.15 K. Throughout the simulations, velocity-rescale thermostat (Nose-Hoover) and constant pressure (1 bar, Parrinello-Rahman NPT ensemble) were adopted. The non-bonded interaction cut-off for electrostatics calculations was set as 10 Å and the particle mesh Ewald (PME) method was used in the calculation of long-range electrostatic interactions with h-bonds LINCS constraints. After reaching equilibrium, *gmx cluster* tool was then applied to extract representative conformations throughout the trajectories. The electrostatic surfaces were calculated by the PyMOL (Schrödinger, LLC.) APBS plugins using AlphaFold2 predicted full-length structural models.

The MicroScale thermophoresis assay (MST)

HSV30, HSV60 and HSV120 were serially diluted with deionized water. Then, 256 nM GFP-pNLRC3 recombinant protein, diluted with a buffer (1 mg/mL BSA, 0.05% Tween 20 in PBS), was incubated with dsDNA of different lengths at room temperature in a total volume of 20 μL. The

mixture was loaded into Monolith NT.115 capillaries. Binding affinity analysis was performed using a NanoTemper Monolith NT.115 instrument, and Kd values were obtained using MO. Affinity Analysis software.

The cGAS activity assay

The full-length pcGAS and the Salmon Sperm DNA (Thermo Fisher, #15632011) or HSV60 (synthesized by Sangon Biotech) were incubated in reaction buffer containing 2 mM GTP, 2 mM ATP, 5 mM $MgCl_2$ and 20 mM HEPES (pH 7.5) for 2 h at 37°C. Samples were centrifuged at 12,000 rpm for 10 min. The supernatant was separated by ultrafiltration and further analyzed by Mono Q ion-exchange column (Cytiva, #17516601) with running buffer containing 50 mM Tris-HCl (pH 8.5) and followed by elution with gradient NaCl running buffer. The production of 2′,3′-cGAMP was analyzed by ion-exchange chromatography.

Animal silhouettes

All animal silhouettes are from PhyloPic and are free of known restrictions or are dedicated to the public domain under the following licenses.

Animal	Creator	License
Human	Yan Wong	Public Domain Mark 1.0
Monkey	T. Michael Keesey	Public Domain Mark 1.0
Lion	T. Michael Keesey	Public Domain Mark 1.0
Pig	Steven Traver	CC0 1.0 Universal Public Domain Dedication
Goat	Steven Traver	CC0 1.0 Universal Public Domain Dedication
Chicken	Steven Traver	CC0 1.0 Universal Public Domain Dedication
Chimpazee	T. Michael Keesey	CC0 1.0 Universal Public Domain Dedication
Baboon	Augustin BROUILLET	CC0 1.0 Universal Public Domain Dedication
Mouse	Tony Goldberg	CC0 1.0 Universal Public Domain Dedication
Deer	Jody Taylor	CC0 1.0 Universal Public Domain Dedication
Duck	Marie Aimée ALLARD	CC0 1.0 Universal Public Domain Dedication

QUANTIFICATION AND STATISTICAL ANALYSIS

Statistical analysis was carried out with GraphPad Prism version 8.0.1. All data were shown as mean ± SD. The mean values for data from each group were compared by Two-tailed unpaired t-test. In all tests, p values of <0.05 were considered statistically significant. ****$p < 0.0001$, ***$p < 0.001$, **$p < 0.01$, *$p < 0.05$. ns, no significance.